Impurity-induced excitations in a topological two-dimensional ferromagnet/superconductor van der Waals moiré heterostructure

Maryam Khosravian[1] and Jose L. Lado[1]

[1]*Department of Applied Physics, Aalto University, 02150 Espoo, Finland*
(Dated: September 27, 2022)

The emergence of a topological superconducting state in van der Waals heterostructures provides a new platform for exploring novel strategies to control topological superconductors. In particular, impurities in van der Waals heterostructures, generically featuring a moire pattern, can potentially lead to the unique interplay between atomic and moire length scales, a feature absent in generic topological superconductors. Here we address the impact of non-magnetic impurities on a topological moire superconductor, both in the weak and strong regime, considering both periodic arrays and single impurities in otherwise pristine infinite moire systems. We demonstrate a fine interplay between impurity induced modes and the moire length, leading to radically different spectral and topological properties depending on the relative impurity location and moire lengths. Our results highlight the key role of impurities in van der Waals heterostructures featuring moire patterns, revealing the key interplay between length and energies scales in artificial moire systems.

I. INTRODUCTION

The design of artificial topological superconductors is one of the most active areas in designer quantum materials[1–15], fueled by their fundamental interest and their potential for future topological computing architectures[16–19]. Engineering topological superconductivity requires three different ingredients magnetism, spin-orbit coupling, and superconductivity, features that have been harvested in a variety of platforms, including semiconducting nanowires[20–22], atomic chains[5,23], topological insulators[24,25], and van der Waals materials[26–28]. In particular, besides all the rich physics of topological superconductors, van der Waals topological superconductors such as $CrBr_3/NbSe_2$ heterostructures[26–28], display a unique feature stemming from their van der Waals nature[29,30], the emergence of a moire pattern.

Artificial van der Waals topological superconductors, and moire heterostructures in general, display two length scales, the original lattice constant and the emergent moire length[31–35]. The existence of a moire pattern leads to a superconducting state with an associated moire electronic structure, and more importantly, a spatially modulated structure directly inherited from the moire pattern[36,37]. In particular, atomic defects in two-dimensional materials including substitutional elements and vacancies have a relevant length scale stemming from the microscopic lattice constant[38–42], and therefore can give rise to a rich interplay with the moire length. While impurities in uniform topological superconductors have been widely studied[43–49], the interplay between local impurities in moire systems has remained relatively unexplored[50–53].

In this manuscript, we address the impact of non-magnetic impurities on artificial moire topological superconductors. We show that interplay between the moire pattern and local impurities gives rise to radically different impacts of the defects depending on the specific location. Our manuscript is organized as follows. First,
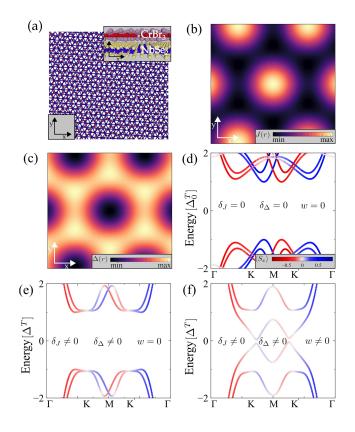

FIG. 1. (a) Schematic view of an artificial $CrBr_3/NbSe_2$ moire topological superconductor. Panels (b,c) show the real-space modulation of exchange coupling $J(\mathbf{r})$ (b) and superconductivity $\Delta(\mathbf{r})$ (c) in the moire unit cell. Panels (d,e,f) electronic band structure of a (d) uniform, (e) moire, and (f) moire with an impurity topological superconductor. We used $J_0=2\Delta_0$, $\lambda=2\Delta_0$, $\mu=3t$, $\delta_J=2J_0$, $\delta_\Delta=1.4\Delta_0$.

in section II we introduce the model for a moire topological superconductor. In Sec. III we address the impact of strong impurities in the topological state. In Sec. IV we address the impact of weak impurities in the moire su-

perconductor. In Sec. V we study the interplay between the amplitude of the moire pattern and the location of the impurity. In Sec. VI we address the emergence of ingap modes for single impurities in otherwise pristine systems. In Sec. VII we examine the emergence of topological moire edge modes in the defective and pristine topological moire superconductor. Finally, in Sec. VIII we summarize our conclusions.

II. MODEL

Here we will consider a generic topological superconductor realized in a van der Waals heterostructure, as realized in a $CrBr_3/NbSe_2$ heterostructure[26]. In this material, the relative lattice mismatch and rotation between the $CrBr_3$ ferromagnet and the $NbSe_2$ superconductor leads to the emergence of a moire pattern, as shown in Fig. 1a. In particular, moire pattern is expected to directly impact underlying Hamiltonian of the system due to the local structural modulation[54–58]. Such a modulation directly imprints Yu-Shiba-Rusinov states following the moire pattern[28]. Due to the structural modulation, including the local hoppings[59], induced spin-orbit coupling[54], chemical potential[60], exchange field[61] and superconducting proximity[62] will be modulated. For the sake of concreteness, here we will focus on the two parameters whose modulation is expected to be most sizable, the local superconducting order and the proximity-induced exchange field. It is worth noting that, beyond the currently realized $CrBr_3/NbSe_2$ heterostructure displaying topological superconductivity[26–28], a variety of other artificial van der Waals systems can potentially lead to topological superconductivity. As two-dimensional ferromagnets, materials such as $CrBr_3$[63], CrI_3[64] and $CrBr_{3-x}I_x$[65], provide potential out-of-plane ferromagnetic monolayers, whereas $NbSe_2$[66], NbS_2[67], TaS_2[68] and $TaSe_2$[69] and their alloys[70] would provide van der Waals superconductors. For all the combinations between ferromagnets and superconductors above, the resulting heterostructure will show a moire pattern between a honeycomb ferromagnet and a triangular superconductor, displaying an approximate C_3 rotational symmetry.

With the previous platforms in mind, we now turn to address a minimal effective model for the previous heterostructures. While the specific parameters of the model for each material combination should be estimated using first-principles calculations[54–58], here we will focus on addressing the universal features that arise due the interplay of the moire superconductor and the local impurities[50–53]. The structure moire pattern directly gives rise to a modulation in the induced exchange coupling and an s-wave superconductivity, whose spatial profiles are shown in Fig. 1bc. The electronic structure of the heterostructure is modeled with an atomistic Wannier orbital per Nb site forming a triangular lattice, where the moire pattern is incorporated in the modulation of the Hamiltonian parameters. The full Hamiltonian takes the form

$$\mathcal{H}_0 = \mathcal{H}_{\text{kin}} + \mathcal{H}_J + \mathcal{H}_R + \mathcal{H}_{\text{SC}} \tag{1}$$

with

$$\mathcal{H}_{\text{kin}} = t \sum_{\langle ij \rangle, s} c_{i,s}^\dagger c_{j,s} + \sum_i \mu(\mathbf{r}) c_{i,s}^\dagger c_{i,s} \tag{2}$$

where $c_{n,s}^\dagger$ ($c_{n,s}$) denotes the creation (annihilation) fermionic operator with spin s in site n. t is the hopping parameter and $\langle i, j \rangle$ runs over nearest neighbors, and μ is the chemical potential. The term

$$\mathcal{H}_J = \sum_{i,s,s'} J(\mathbf{r}) \sigma_z^{s,s'} c_{i,s}^\dagger c_{i,s'} \tag{3}$$

is the exchange coupling induced by the underlying ferromagnet, obtained by integrating out the degrees of freedom of the magnetic monolayer. The term

$$\mathcal{H}_R = i\lambda \sum_{\langle ij \rangle, ss'} \mathbf{d}_{ij} \cdot \sigma^{s,s'} c_{i,s}^\dagger c_{j,s'} \tag{4}$$

is the Rashba spin-orbit coupling arising due to the broken mirror symmetry at the $NbSe_2/CrBr_3$ interface, σ are the spin Pauli matrices, λ controls the spin-orbit coupling constant and $\mathbf{d}_{ij} = \mathbf{r}_i - \mathbf{r}_j$. The term

$$\mathcal{H}_{\text{SC}} = \sum_i \Delta(\mathbf{r}) c_{i,\uparrow}^\dagger c_{i,\downarrow}^\dagger + h.c. \tag{5}$$

is the s-wave superconducting order. $J(\mathbf{r})$ and $\Delta(\mathbf{r})$ parameterize the exchange coupling and induced s-wave superconductivity.

Local non-magnetic impurities are included adding a potential scattering term of the form

$$\mathcal{H}_{\text{imp}} = w \sum_s c_{n,s}^\dagger c_{n,s} \tag{6}$$

where $\mathcal{H}_{\text{imp}}$ defines the impurity Hamiltonian at site n with an on-site potential w. The full Hamiltonian of the defective system takes the form

$$\mathcal{H} = \mathcal{H}_0 + \mathcal{H}_{\text{imp}} \tag{7}$$

As noted above, the moire profile in our effective model arises from the combination of modulated exchange coupling and s-wave superconductivity[71]. The interplay between the exchange field and the superconducting order, as two competing orders, results in an opposite modulated superconductivity and therefore exhibits a modulated moire pattern in the whole platform. We account

for this by defining a potential in real space with the functional form of

$$f(\mathbf{r}) = c_0 + c_1 \sum_{n=1}^{3} \cos(R^n \mathbf{q} \cdot \mathbf{r}) \qquad (8)$$

where $\mathbf{q}$ is the moire superlattice wave vector, and R_n is the rotation matrix which conserve C_3 symmetry and c_0, c_1 are chosen so that $f(\mathbf{r}) \in (0,1)$. The spatial profiles $J(\mathbf{r})$ and $\Delta(\mathbf{r})$ are written in terms of the previous spatial dependence as

$$J(\mathbf{r}) = J_0 + \chi \delta_J f(\mathbf{r})$$
$$\Delta(\mathbf{r}) = \Delta_0 + \chi \delta_\Delta (1 - f(\mathbf{r})) \qquad (9)$$

J_0 and Δ_0 controls the average magnitude of the modulated exchange and superconducting profiles, whereas δ_J and δ_Δ control the amplitude of the moire modulation, respectively. We introduce $\chi \in (0,1)$ as a parameter which allows us to adiabatically switch between a uniform or moire system, and here it is taken to be 1. As noted above, the relative signs of $f(\mathbf{r})$ in $J(\mathbf{r})$ and $\Delta(\mathbf{r})$ are taken so that when the exchange is maximum, the local superconducting order is minimum. We now elaborate on the mechanism that yields those two parameters as the dominating modulations. The stacking heavily influences the value of the exchange, and ultimately it can also impact its sign[72,73]. This strong modulation of the exchange directly affects the local superconducting order, as a finite exchange field locally quenches the s-wave pairing. Therefore the superconducting and exchange modulations are anticorrelated. This is the behavior directly expected from the pair-breaking effect of the exchange field in an s-wave superconductor[74,75], and arises naturally from a selfconsistent treatment of the superconducting state in the presence of the moire modulated exchange. Experimentally, the impact of moire modulations in $NbSe_2/CrBr_3$ has been directly observed by imaging the spatial dependence of the Yu-Shiba-Rusinov (YSR) bands at energies inside the gap, directly reflecting the modulation of the exchange coupling[28]. We note that, for the superconductor taken as $NbSe_2$, the closest saddle point to the Fermi energy that will have the strongest moire effect is located at the M point[76]. Finally, of course the moire can also influence the other parameters, but their effect is expected to be be substantially smaller in comparison with the exchange field.

We now briefly elaborate in the procedure to solve the previous Hamiltonian. We take as starting point the effective Hamiltonian for a periodic moire supercell, that takes the form

$$\mathcal{H} = \sum \Gamma_{i,j,s,s'}^{\alpha,\beta} c_{i,\alpha,s}^\dagger c_{j,\beta,s'} + \sum (\Delta_\alpha c_{i,\alpha,\uparrow}^\dagger c_{i,\alpha,\downarrow}^\dagger + h.c.) \qquad (10)$$

where $c_{i,\alpha,s}^\dagger$ denotes the creation operator at unit cell i, site α and spin s and $\Gamma_{i,j,s,s'}^{\alpha,\beta}$ contains the hopping,

spin-orbit coupling and exchange proximity effects. The previous Hamiltonian, periodic in the supercell, can be diagonalized by defining the Bloch's operators

$$c_{j,\alpha,s} = \sum_{\mathbf{k}} e^{i\mathbf{k}\cdot\mathbf{R_j}} c_{\mathbf{k},\alpha,s} \qquad (11)$$

leading to the Hamiltonian in momentum space

$$\mathcal{H} = \sum \Gamma_{s,s'}^{\alpha,\beta}(\mathbf{k}) c_{\mathbf{k},\alpha,s}^\dagger c_{\mathbf{k},\beta,s'} + \sum [\Delta_\alpha c_{\mathbf{k},\alpha,\uparrow}^\dagger c_{-\mathbf{k},\alpha,\downarrow}^\dagger + h.c.] \qquad (12)$$

where $\Gamma_{s,s'}^{\alpha,\beta}(\mathbf{k})$ is the Fourier transform in the unit cell indexes i,j of the matrices $\Gamma_{i,j,s,s'}^{\alpha,\beta}$. To diagonalize the previous Hamiltonian, we define a new fermionic operators $c_{\mathbf{k},s}^\dagger \equiv (c_{\mathbf{k},1,s}^\dagger, ..., c_{\mathbf{k},n,s}^\dagger)$ and $\Psi_{\mathbf{k}}^\dagger = (c_{\mathbf{k},\uparrow}^\dagger, c_{\mathbf{k},\downarrow}^\dagger, c_{-\mathbf{k},\downarrow}, c_{-\mathbf{k},\uparrow})$. The Hamiltonian in this basis can be written as

$$\mathcal{H} = \frac{1}{2} \sum \Psi_{\mathbf{k}}^\dagger H_{BdG} \Psi_{\mathbf{k}} \qquad (13)$$

where the Bogoliubov de Gennes (BdG) Hamiltonian H_{BdG} is diagonalized in terms of the new operators, leading to a diagonal form

$$\mathcal{H} = \frac{1}{2} \sum \epsilon_{\mathbf{k},\alpha} \Psi_{\mathbf{k},\alpha}^\dagger \Psi_{\mathbf{k},\alpha} \qquad (14)$$

where $\epsilon_{\mathbf{k},\alpha}$ are the BdG eigenvalues and $\Psi_{\mathbf{k},\alpha}^\dagger$ the BdG eigenstates.

In practice, the calculation of the electronic structure for a moire supercell requires diagonalizing a $4n \times 4n$ matrix, with n the number of sites per supercell. To compute the electronic structure in a ribbon geometry, an analogous procedure as the one outline above is carried out for the supercell of the nanoribbon, that contains several moire unit cells. Finally, to compute surface spectral functions, the embedding formalism described later in the manuscript is directly applied to the matrices defined by the BdG Hamiltonian.

It is instructive to first look at the electronic structure and topological character of the uniform system of Eq. 1 when moire potential is switched off. For the Hamiltonian parameters we choose the following setup: $J_0{=}2\Delta_0$, $\lambda{=}2\Delta_0$, and the chemical potential set to $\mu = 3t$. In the uniform limit, for a supercell of size 9×9 as shown in Fig. 1d, the system shows a finite gap of topological character, where the energy is measured in terms of the topological gap of the uniform system Δ_0^T. This topological superconducting gap is obtained by taking appropriate ratios of the exchange field, Rashba spin-orbit coupling, superconducting order and chemical potential, and features a topological gap with Chern number $C = 2$[26].

Keeping the same average values of the exchange, superconductivity, Rashba spin-orbit coupling and chemical potential, we now move on to the moire system, switching on the exchange and superconducting modulation δ_J and δ_Δ, which are set to $\delta_J{=}2J_0$, $\delta_\Delta{=}1.4\Delta_0$. The

electronic structure of the modulated system is shown in Fig. 1e, and features a topological gap with Chern number $C = 2$, where the energy is measured in terms of the topological gap of the moire system Δ^T. We note that there is not a simple analytic relation between both gaps, and in our calculations we explicitly compute both. Phenomenologically, in the regime we will target we find that the moire modulation slightly decreases the topological gap, in the worst case scenario by up to a factor three in comparison with the uniform case. In this last moire superconductor, we now consider the impact of a single strong non-magnetic impurity per moire unit cell with $w = 2t$. The electronic structure of the moire modulated system with a single impurity is shown in Fig. 1f. It is clearly observed that the gap gets drastically reduced in comparison with the moire pristine limit of Fig. 1e. The dramatic impact of the local impurity is a consequence of the unconventional nature of the topological superconducting gap of the moire heterostructure. While this feature also appears in generic artificial topological superconductors[43–49], the existence of the moire pattern gives rise to a complex interplay between the local impurity and the moire length as we address in the next sections.

III. STRONG IMPURITIES IN TOPOLOGICAL MOIRE SUPERCONDUCTORS

We now examine in detail the case of a strong impurity potential. Strong impurities in the effective model are associated to chemical impurities[41,77–79] and vacancies[80] in the dichalcogendie superconductor, and give rise to a strong scattering center. In particular, for the dichalcogenide superconductor, chemical impurities such as oxygen[42] will give rise to a strong disruption of the electronic structure. Substitutional oxygen impurities, in particular, are expected to create a strong local scattering, comparable and even higher than the hopping of the low energy Wannier orbitals[78]. In contrast, atomic replacements such as substitutional S atoms in $NbSe_2$ and $TaSe_2$ would give rise to weaker scattering centers[70,81].

It is worth noting that, since the scattering potential induced by the previous impurities is non-magnetic, the emergence of in-gap modes stems from the non-trivial nature of the superconducting gap in the moire system[43]. In particular, non-magnetic impurities in conventional s-wave superconductors are well known to not give rise to in-gap states as given by Anderson's theorem[82–85]. In contrast, topological superconductors with non-zero Chern number feature in-gap modes in the presence of non-magnetic impurities, rendering artificial topological superconductors vulnerable to disorder[86–89]. This weakness to disorder stems from the fact that non-magnetic scattering has a pair breaking effect[43,83] in unconventional superconductors due to the non-trivial sign structure of the superconducting order[84].
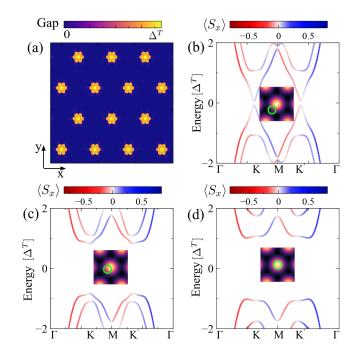

FIG. 2. (a) Gap as a function of impurity location in the strong impurity regime $w = 2t$. Panels (bcd) show the electronic structure for three impurity locations, showing that halfway between exchange maxima, the gap is minimal (b). In comparison, close to the exchange maxima, the gap remains nearly unchanged (c,d). We used $J_0 = 2\Delta_0$, $\lambda = 2\Delta_0$, $\mu = 3t$, $\delta_J = 2J_0$, $\delta_\Delta = 1.4\Delta_0$.

It is first instructive to examine the gap of the moire system as a function of the location of a strong impurity ($w = 2t$) in a 9×9 supercell, as shown in Fig. 2a. We focus here on the case with a periodic array of impurities in the system following the moire pattern, with a single impurity per moire unit cell, and we keep the same parameters values as we have introduced in section II. Fig. 2a shows the full gap of the moire pattern, for a single impurity per moire unit cell located at each potential location. The gap is measured in units of the topological gap for the topological pristine system Δ^T. In particular, it is observed that the location of the impurity strongly impacts the gap of the system[90]. The resulting gap of the defective system can range from the pristine value, observed for impurities at the exchange maximum, to nearly zero, observed for impurities away from the exchange maximum (Fig. 2a). The previous phenomenology is directly reflected in the electronic band structure for different locations of the impurity (Fig. 2bcd). The electronic structure for an impurity halfway between two exchange maxima is shown in Fig. 2b, which in particular shows a dramatically smaller gap than the pristine system. In stark contrast, for two locations of the impurities close to the exchange maxima as shown in Fig. 2cd, the gap of the system remains nearly the same as in the pristine system. In particular, the system retains its topologically non-trivial Chern number $C = 2$ with a nearly

identical gap for the central impurities shown in Fig. 2cd, whereas the gap is drastically reduced for the location of Fig. 2b.

The previous phenomenology highlights that the location of the non-magnetic impurity in the moire pattern has a critical impact on the superconducting gap of the system. Such strong spatial dependence is fully absent both in non-topological moire superconductors due to Anderson's theorem[82], as well as in non-moire artificial topological superconductors due to the equivalence of the sites.

It is interesting noting that in a moire superconductor there is a large mismatch between the length scales of the Bloch states and the impurity, in comparison with a uniform superconductor. While there is certainly a mismatch of length scales, our results show that the effect of impurities is comparable both in the absence and presence of a moire. From the low energy point of view, a local impurity in real space can be considered like a delta function potential, which creates scattering between all wavevectors in reciprocal space. In the presence of a moire, the minibands span a small portion of the original Brillouin zone of the material. Nonetheless, due to the mixing between all wavevectors driven by a local impurity, its effect in the minibands is comparable.

IV. WEAK IMPURITIES IN TOPOLOGICAL MOIRE SUPERCONDUCTORS

In this section, we examine the electronic structure of the moire modulated model when a periodic array of weak impurities is distributed in the unit cell, with a single impurity per moire unit cell. In particular, we examine the evolution of the gap as a function of the impurity location, which highlights the fine interplay between the moire length and atomic defect. It is worth noting that examining the gap for weak impurities allows tracking small changes in the gap as a function of the impurity location, guaranteeing that the system remains in a topological phase. As noted above, weak impurities would correspond to chalcogen substitution, such as S in $NbSe_2$, leading to a local potential smaller than the bandwidth of the low energy states.

We first look at the map of the spectral gap as a function of impurity location. We take a moire unit cell with the size of 9×9, as shown in Fig 3a. It is observed that similar to the strong impurity regime of Sec. III, the gap remains maximal close to the maximum of the exchange profile, becoming smaller in the other locations of the moire unit cell. In comparison with the strong impurity limit, the weak impurity allows keeping a sizable topological gap even for the most detrimental locations away from the exchange maxima. The previous phenomenology can also be observed by examining the electronic structure for different locations of the impurity, shown in Figs. 3bcd. In particular, it is observed that the electronic structure remains similar for the three impurity
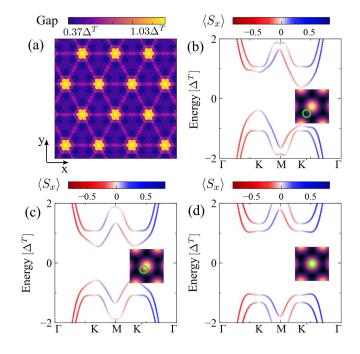

FIG. 3. (a) Gap as a function of impurity location in the weak impurity regime $w = t/2$. Panels (bcd) show the electronic structure for three impurity locations, showing that halfway between exchange maxima, the gap is minimal (b). In contrast, close to the exchange maxima, the gap remains nearly unchanged (c,d). We used $J_0=2\Delta_0$, $\lambda =2\Delta_0$, $\mu = 3t$, $\delta_J = 2J_0$, $\delta_\Delta = 1.4\Delta_0$.

locations, apart from small rearrangements that account for the reduced topological gap.

The previous spatial dependence for different impurity locations can be analyzed as a function of the moire length. The gap for a single impurity per moire unit cell, computed for different moire lengths is shown in Fig. 4, where we consider 11×11 (Fig. 4a), 13×13 (Fig. 4b), 15×15 (Fig. 4c) and 17×17 (Fig. 4d). In particular, we observe that close to the exchange maxima, the local impurity has a relatively weak impact, with the exception of the exact center. Away from the exchange maxima, the impurity shows some of the most sizable effects, having also a complex dependence with the moire length. This complex dependence naturally emerges from the interplay of between the moire length and the spatial dependence of the in-gap mode, and is intrinsic to any non-magnetic impurity in a moire topological superconductor. In particular, the interference between the in-gap state and the moire pattern will be further addressed in Sec. VI, where we will consider a single impurity in an otherwise pristine moire system.

In this section, we have focused on addressing the fine interplay between a periodic array of impurities and the moire pattern. In particular, it is observed a dramatic dependence of the spectral gap on the location of the impurity, directly correlated with the underlying moire pattern. In contrast with the strong impurity case, weak
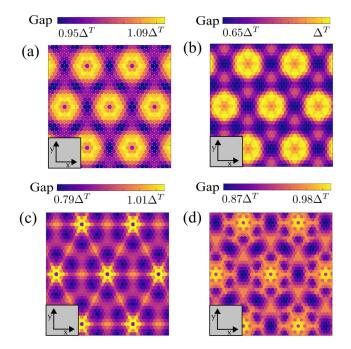
FIG. 4. Topological gap as a function of the location of an impurity in a the moire unit cell, for (a) 11×11, (b) 13×13 (c) 15×15 (d) 17×17 supercells. It is observed a direct correlation between the location of the impurity in the unit cell and the moire pattern, leading to drastic changes in the energy gap. We used $J_0=2\Delta_0$, $\lambda =2\Delta_0$, $\mu = 3t$, $\delta_J = 2J_0$, $\delta_\Delta = 1.4\Delta_0$.
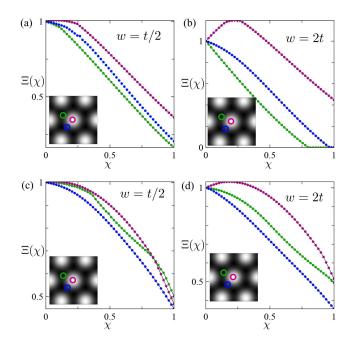

FIG. 5. Normalized topological gap as a function of moire amplitude (Eq. 15) for weak (a,c) and strong (b,d) impurity, for a 9×9 (a,b) and a 11×11 (c,d) moire. It is observed that in the absence of the moire the location of the impurities does not impact the magnitude of the gap, whereas with moire, the topological gap shows a strong dependence on the size and location of the impurity. We used $J_0=2\Delta_0$, $\lambda =2\Delta_0$, $\mu = 3t$.

impurities will keep the topological gap unchanged, and in particular, all the defective superconducting states of this section show the pristine Chern number $C = 2$.

V. IMPACT OF THE MOIRE AMPLITUDE

In a moire superconductor, the moire pattern is characterized by the amplitude of the modulation and its average value. In this section, we analyze in detail the effect of moire amplitude, allowing us to interpolate from the uniform to the modulated limit. In particular, in the uniform limit, the location of the impurity in the unit cell must lead to identical gaps. In contrast, as the moire pattern is switched on, the gap in the presence of an impurity will develop a strong dependence on its location. To track the evolution with the moire pattern, we

keep the average values of the exchange and superconductivity constant, as well as keeping constant ratios of their modulated amplitude and vary the χ parameter, defined in Eq. 9, between 0 and 1 ,which allows interpolating between the uniform and moire limit.

The topological gap for different locations of the impurity and moire unit cells as a function of the moire amplitude is shown in Fig. 5. We consider two different moire unit cells, a 9×9 moire unit cell (Fig. 5ab) and a 11×11 moire unit cell (Fig. 5cd), and two strengths of the impurity $w = t/2$ (Fig. 5ac) and $w = 2t$ (Fig. 5bd). For

different locations of the impurities, we compute the gap of the moire system normalized to the gap of a uniform system with impurities.

$$\Xi(\chi) = \frac{\mathcal{G}(\chi,w)}{\mathcal{G}(\chi = 0, w)} \tag{15}$$

where $\mathcal{G}$ is the gap of the system. The ratio $\Xi(\chi)$ allows to directly observe the dependence on the location of the impurity for different moire modulations.

We now focus on the three locations of the impurities shown in Fig. 5, one close to the exchange maximum of the moire (red), halfway between two exchange maxima (blue), and close to the center formed by three exchange maxima (green). In the absence of a moire modulation, the three locations lead to the same topological gap, while as the moire χ is turned on, the gap shows a dependence on the location. In particular, we observe that in most of the instances, the biggest gap is obtained for an impurity close to the exchange maxima (Fig. 5), consistent with the results obtained in Fig. 4. For the locations away from the exchange maxima, the gap is maximized for different locations depending on the moire length, as it is observed by comparing Fig. 5a with Fig. 5c, and Fig. 5b with Fig. 5d. This phenomenology is also consistent with the moire dependence observed in Fig. 4. It is worth noting that, as long as the gap remains open, the Chern number will remain the same all the time. It
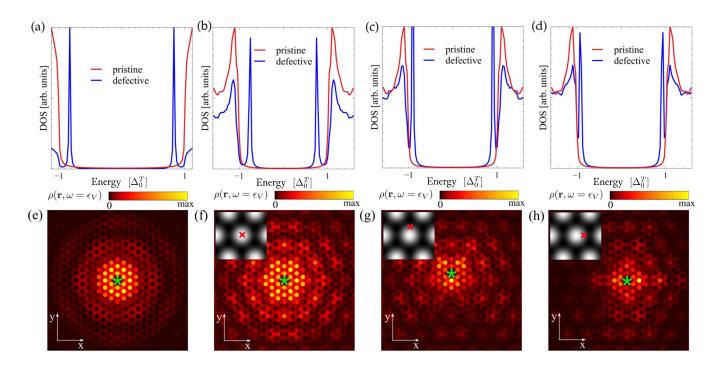
FIG. 6. Density of states (a-d) and local density of states (e-h) at the energy of the ingap state ϵ_V for a single impurity in an otherwise pristine system. Panels (a,e) correspond to the uniform case, whereas panels (b,c,d,f,g,h) to different locations of a single impurity (insets in f,g,h) for the moire case Both in the absence (a) and presence (b,c,d) of a moire, a strong non-magnetic impurity gives rise to an in-gap state. It is observed that in the presence of the moire pattern, the in-gap state leads to a strong interference with moire length, yielding a spatial dependence with respect to the location of the impurity (f,g,h). We used $J_0=2\Delta_0$, $\lambda =2\Delta_0$, $\mu = 3t$, $\delta_J = 2J_0$, $\delta_\Delta = 1.4\Delta_0$ and moire 5×5.

is finally interesting to note that, for a strong impurity, the location in the moire unit cell leads to substantially bigger changes in the gap than a weak impurity. This phenomenology is consistent with the results observed in Fig. 2 and Fig. 3.

The previous findings highlight that, in the presence of a moire modulation, the location of an impurity leads to different gaps, especially in the strong coupling limit. Beyond the cases shown in Fig. 4, we note that even at the center of the unit cell, strong impurities can give rise to a strong impact in the topological phase and ultimately lead to a topological phase transition. For other locations, the topological gap shows a complex interplay between the location of the impurity and the moire length. These results consider a single impurity per moire unit cell, leading to strong overlap and interference between each in-gap mode.

We finally comment on what would be the impact if disorder is included in every single site. In such limit, as the strength of the disorder increases, the value of the topological gap will decrease. For weak disorder, the gap will remain finite, yet smaller than the non-disordered case. However, for strong enough uniform disorder, the system will effectively become gapless due to pair breaking effect of the impurities. This phenomenology is analogous to other unconventional non-swave superconductor, where non-magnetic disorder quenches the underly-

ing topological superconducting gap.

VI. SINGLE IMPURITY LIMIT

In the sections above, we have focused on considering a periodic array of impurities in the moire system. Here we will focus on a complimentary limit, namely the case of a single impurity on an otherwise pristine moire system. In this case, the moire system with a single impurity will lack any type of translational symmetry, and therefore an electronic bandstructure associated with a moire Bloch's theorem can not be computed. In order to study the single impurity limit, we will use Green's function embedding method, which allows to compute exactly single defects in otherwise infinite pristine systems[91,92].

The embedding method relies on writing down the Dyson equation for the defective system, that takes the form

$$G_V(\omega) = [\omega - H_V - \Sigma(\omega) + i0^+]^{-1} \qquad (16)$$

where $G_V(\omega)$ is the Green's function of the defective model, H_V the Hamiltonian of the defective unit cell, and $\Sigma(\omega)$ the selfenergy induced by the rest of the pristine system. Solving the previous equation requires deriving

the selfenergy of the pristine system $\Sigma(\omega)$. The selfenergy $\Sigma(\omega)$ can be obtained by writing down the Dyson equation for the pristine model

$$G_0(\omega) = [\omega - H_0 - \Sigma(\omega) + i0^+]^{-1} \qquad (17)$$

with H_0 the Hamiltonian of the pristine unit cell. We can now take Bloch's representation of the pristine unit cell Green's function

$$G_0(\omega) = \frac{1}{(2\pi)^2} \int [\omega - H_{\mathbf{k}} + i0^+]^{-1} d^2\mathbf{k} \qquad (18)$$

where $H_{\mathbf{k}}$ is the Bloch's Hamiltonian. By obtaining G_0 from Eq. 18, the selfenergy $\Sigma(\omega)$ can be obtained from Eq. 17, which in turn allows to obtain the Green's function of the defective unit cell from Eq. 16.

Using the previous methodology, we can extract both the total and local density of states for a single defect in the moire topological superconductor. The local density of states $\rho(\mathbf{x}, \omega)$ and full density of states $A(\omega)$ are obtained as

$$\rho(\mathbf{x}, \omega) = -\frac{1}{\pi} \sum_{s,\tau} \langle \mathbf{x}, s, \tau | \text{Im}(G_V(\omega)) | \mathbf{x}, s, \tau \rangle \qquad (19)$$

and

$$\rho(\omega) = -\frac{1}{\pi} \text{Tr}[\text{Im}(G_V(\omega))] \qquad (20)$$

where s runs over spin and τ over electron-hole sector. With the previous methodology, we now compute the density of states with a single impurity for the topological superconductor without moire pattern (Fig. 6).

It is first instructive to consider the impurity in the uniform topological superconductor, shown in Figs. 6ae. In particular, it is observed that the existence of a strong non-magnetic impurity ($w = 2t$) gives rise to an in-gap state (Fig. 6a), and that the spatial profile of such in-gap mode is localized around the impurity (Fig. 6e) and features intensity oscillations in space. These results in the uniform limit directly suggest that the moire pattern will give rise to a rich interference pattern with the in-gap state, ultimately responsible for the strong dependence of the location of the impurity observed in previous sections.

We now move on to consider the case with a finite moire pattern and single impurity, whose density of states is shown in Figs. 6bcd and the local density of states is shown in Figs. 6fgh, for different location of the impurity with respect to the center of the moire pattern, shown by the insets in fgh. In particular, we consider three different locations of the impurities. As shown in Fig. 6bcd for all the locations of the impurities, we observe in-gap modes at energies ϵ_V. When computing the local density of states associated with those in-gap modes ϵ_V, shown in Figs. 6fgh, it is observed that the interference

pattern between the bound state and the moire pattern leads to a strong dependence depending on the location of the impurity[93]. Furthermore, it observed that the in-gap mode spans over several moire unit cells, highlighting that for the periodic array considered in the sections above the in-gap modes between different unit cells have a strong overlap.

The previous results highlight that impurities in the moire pattern give rise to in-gap states whose wavefunctions can potentially span over several unit cells, and lead to strong interference effects with the moire modulation. The previous phenomenology accounts for the strong dependence of the topological gap as a function of the impurity location observed in Sec. IV and Sec. III.

VII. EDGE STATES

Finally, we analyze the emergence of edge states associated with the moire topological superconducting state in a ribbon with the structure, inset in Fig. 7d,h, displaying a schematic of the boundary conditions, which is periodic along x direction and finite along y direction.

In particular, we will consider both pristine and defective cases, and show that in both instances, the edge modes reflect the underlying moire pattern. We first take a pristine system displaying the moire topological superconducting state, as shown in Figs. 7abcd. The electronic structure of a ribbon, infinite in the x-direction, is shown in Fig. 7a, displaying both the existence of a gap in the bulk and propagating edge modes. Those two features are more clearly seen by computing the edge (Fig. 7b) and bulk (Fig. 7c) spectral functions as shown in Fig. 7bc. $A(\mathbf{k}, \omega)$ is the momentum-resolved spectral function in the surface and bulk of a semi-infinite ribbon, with $\mathbf{k}$ the momentum in the translational invariant direction of the ribbon. It is computed from the momentum-resolved Green's function as $A(\mathbf{k}, \omega) = -\frac{1}{\pi} \text{Tr}[\text{Im}(G(\mathbf{k}, \omega))]$ where $G(\mathbf{k}, \omega)$ is computed with a renormalization algorithm[94]. In particular, it is observed that the edge hosts two co-propagating modes (Fig. 7b), consistent with the electronic structure of the moire ribbon of Fig. 7a. Beyond the existence of edge modes, the moire pattern gives rise to a unique feature in real space, namely the modulation of the edge modes following the moire pattern. This can be clearly seen in Fig. 7d, where it is observed that the zero-energy modes directly reflect the underlying moire pattern in the Hamiltonian.

We now move on to consider the defective system. In particular, we focus on a moire superconductor with a single strong impurity per moire unit cell. We emphasize that, depending on the location of the impurity and the moire length, the topological phase can remain the same, become gapless, or a topological phase transition can take place. For the sake of concreteness, here we take a location of an impurity that strongly disrupts the original topological state, giving rise to a topological
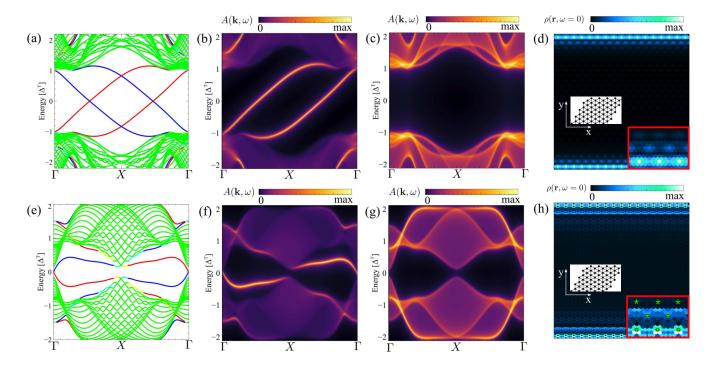
FIG. 7. Moire topological superconducting states of a pristine system (a,b,c,d) and of a defective system (e,f,g,h). Panels (a,e) show the electronic structure of a ribbon infinite in the x direction and finite in the y direction. Panels (b,f) show the momentum-resolved edge spectral function, and panels (c,g) the momentum-resolved bulk spectral function. Panels (d,h) show the local density of states at $\omega = 0$, highlighting the emergence of topological zero modes at the top and bottom edges following the moire pattern. The structure insets in (d,h) show a schematic of the boundary conditions used. We used $J_0=2\Delta_0$, $\lambda =2\Delta_0$, $\mu = 3t$, $\delta_J = 2J_0$, $\delta_\Delta = 1.4\Delta_0$, and moire 5×5.

phase transition to a phase with Chern number $C = -1$. The electronic structure of the defective ribbon is shown in Fig. 7e, where it observed the existence of a small bulk gap and edge modes. Those modes can be more clearly observed by computing the edge (Fig. 7f) and bulk (Fig. 7g) spectral function as shown in Figs. 7fg. In particular, the edge spectral function now displays a single edge mode as shown in Fig. 7f, as expected from the bulk Chern number $C = -1$. It is also observed that the topological edge states avoid the location of the impurity, marked with a green star in Fig. 7f, as expected from the strong impurity limit. The edge modes reflect the moire periodicity again as shown in Fig. 7h, leading to the imprinting of the moire pattern in the topological edge modes.

The defective case considered above focuses on a periodic array of strong impurities. In real experiments, impurities can appear either randomly distributed or can be engineered in arrays using atomic manipulation. The first case would correspond to chemical impurities intrinsically appearing during synthesis of the material. In this situation, depending on the density of impurities and their respective location, the original moire topological phase will be disrupted, either by decreasing its topological gap or ultimately by leading to a gapless state due to the proliferation of in-gap modes. In the situation in which a periodic array of impurities is engi-

neered by means of atomic manipulation[95–105], specific arrangements as those considered in Fig. 7efgh can give rise to a topological state with different Chern number. We have verified that solely by changing the location in which the impurity is deposited in the moire unit cell, the resulting electronic structure could result in topological phases with different Chern number, trivial phases, or even gapless phases. The previous results highlight that atomic manipulation on top of moire topological superconductors provides a new potential degree of freedom to engineer tunable topological superconductors[106], by exploiting the interplay between the moire length and local impurities[50–53].

We finally note that this analysis focuses on a minimal model that accounts for the physics of van der Waals ferromagnet/superconductor heterostructures[26–28]. From the quantum chemistry point of view, our model does not account for all the microscopic parameters, but rather focuses on an effective model capturing the physics of this family of heterostructures. In order to provide a microscopically accurate description, calculations would need to be carried out with Wannierization procedures based on first principles density functional methods[107]. In particular, these methodologies would account for the modulations in all the Hamiltonian parameters, including spin-orbit coupling, hoppings, and onsite energies. Furthermore, relaxation effects would be directly captured

with these methodologies[107]. We note, however, that for the current system, first-principles density functional theory methodologies are beyond the computational capabilities, in particular in the presence of spin-orbit coupling, due to the large number of atoms in the unit cell for such a moire structure. As a results, our discussions focus on a model Hamiltonian, yet without aiming to reach chemical accuracy for $NbSe_2/CrBr_3$ heterostructures.

VIII. CONCLUSION

To summarize, here we addressed the interplay between local impurities and moire effects in topological moire superconductors, as those realized in $CrBr_3/NbSe_2$ heterostructures. In particular, our results highlight that, in contrast with conventional artificial topological superconductors, the impact of impurities on a moire system can give rise to radically different properties depending on their location in the moire pattern. For strong impurities, we observed that solely depending on the location of the impurity in the moire pattern, the electronic structure can show as similar topological gap as in the pristine limit, a nearly gapless state or a topological phase transition to a topologically different state. For weak impurities, we showed that the topological superconducting gap shows a dependence both on the location of the impurity and the moire length, yet maintaining its topological nature for all locations. Furthermore, using an embedding formalism we addressed the impact of single non-magnetic impurities in otherwise infinite pristine moire systems. In particular, the absence of interference between impurities allows to clearly identify that the moire modulation drastically impacts the spatial profile of the in-gap mode created by the non-magnetic scatterer. Ultimately, we showed that the moire modulation further emerges in the topological edge modes of the topological superconductor, both in the pristine moire limit and the defective limit. Our results highlight the rich interplay between local impurities and topological moire superconductors, and put forward engineered atomic impurities as a powerful and versatile strategy to engineer artificial van der Waals moire topological superconductors.

1 C.W.J. Beenakker, "Search for majorana fermions in superconductors," Annual Review of Condensed Matter Physics **4**, 113–136 (2013).

2 Fan Zhang, C. L. Kane, and E. J. Mele, "Time-reversal-invariant topological superconductivity and majorana kramers pairs," Phys. Rev. Lett. **111**, 056402 (2013).

3 Jason Alicea, Yuval Oreg, Gil Refael, Felix von Oppen, and Matthew P. A. Fisher, "Non-abelian statistics and topological quantum information processing in 1d wire networks," Nature Physics **7**, 412–417 (2011).

4 Benjamin E. Feldman, Mallika T. Randeria, Jian Li, Sangjun Jeon, Yonglong Xie, Zhijun Wang, Ilya K. Drozdov, B. Andrei Bernevig, and Ali Yazdani, "High-resolution studies of the majorana atomic chain platform," Nature Physics **13**, 286–291 (2016).

5 S. Nadj-Perge, I. K. Drozdov, J. Li, H. Chen, S. Jeon, J. Seo, A. H. MacDonald, B. A. Bernevig, and A. Yazdani, "Observation of majorana fermions in ferromagnetic atomic chains on a superconductor," Science **346**, 602–607 (2014).

6 Falko Pientka, Leonid I. Glazman, and Felix von Oppen, "Topological superconducting phase in helical shiba chains," Phys. Rev. B **88**, 155420 (2013).

7 Kim Pöyhönen and Teemu Ojanen, "Superlattice platform for chiral superconductivity with tunable and high chern numbers," Phys. Rev. B **96**, 174521 (2017).

8 Joel Röntynen and Teemu Ojanen, "Topological superconductivity and high chern numbers in 2d ferromagnetic shiba lattices," Phys. Rev. Lett. **114**, 236803 (2015).

9 A. R. Akhmerov, Johan Nilsson, and C. W. J. Beenakker, "Electrically detected interferometry of majorana fermions in a topological insulator," Phys. Rev. Lett. **102**, 216404 (2009).

10 Doru Sticlet, Cristina Bena, and Pascal Simon, "Spin and majorana polarization in topological superconducting wires," Phys. Rev. Lett. **108**, 096802 (2012).

11 Jelena Klinovaja, Peter Stano, Ali Yazdani, and Daniel Loss, "Topological superconductivity and majorana fermions in rkky systems," Phys. Rev. Lett. **111**, 186805 (2013).

12 J. L. Lado and M. Sigrist, "Two-dimensional topological superconductivity with antiferromagnetic insulators," Phys. Rev. Lett. **121**, 037002 (2018).

13 Andreas Kreisel, Timo Hyart, and Bernd Rosenow, "Tunable topological states hosted by unconventional superconductors with adatoms," Phys. Rev. Research **3**, 033049 (2021).

14 P. San-Jose, J. L. Lado, R. Aguado, F. Guinea, and J. Fernández-Rossier, "Majorana zero modes in graphene," Phys. Rev. X **5**, 041042 (2015).

15 Xiao-Liang Qi and Shou-Cheng Zhang, "Topological insulators and superconductors," Rev. Mod. Phys. **83**, 1057–1110 (2011).

16 Jason Alicea, "New directions in the pursuit of majorana fermions in solid state systems," Reports on Progress in Physics **75**, 076501 (2012).

17 David Aasen, Michael Hell, Ryan V. Mishmash, Andrew Higginbotham, Jeroen Danon, Martin Leijnse, Thomas S. Jespersen, Joshua A. Folk, Charles M. Marcus, Karsten Flensberg, and Jason Alicea, "Milestones toward majorana-based quantum computing," Phys. Rev. X **6**, 031016 (2016).

18 Jay D. Sau, Roman M. Lutchyn, Sumanta Tewari, and S. Das Sarma, "Generic new platform for topological

quantum computation using semiconductor heterostructures," Phys. Rev. Lett. **104**, 040502 (2010).

[19] Yuval Oreg, Gil Refael, and Felix von Oppen, "Helical liquids and majorana bound states in quantum wires," Phys. Rev. Lett. **105**, 177002 (2010).

[20] V. Mourik, K. Zuo, S. M. Frolov, S. R. Plissard, E. P. A. M. Bakkers, and L. P. Kouwenhoven, "Signatures of majorana fermions in hybrid superconductor-semiconductor nanowire devices," Science **336**, 1003–1007 (2012).

[21] M. T. Deng, S. Vaitiekėnas, E. B. Hansen, J. Danon, M. Leijnse, K. Flensberg, J. Nyg**r**ard, P. Krogstrup, and C. M. Marcus, "Majorana bound state in a coupled quantum-dot hybrid-nanowire system," Science **354**, 1557–1562 (2016).

[22] Anindya Das, Yuval Ronen, Yonatan Most, Yuval Oreg, Moty Heiblum, and Hadas Shtrikman, "Zero-bias peaks and splitting in an al–InAs nanowire topological superconductor as a signature of majorana fermions," Nature Physics **8**, 887–895 (2012).

[23] Lucas Schneider, Philip Beck, Thore Posske, Daniel Crawford, Eric Mascot, Stephan Rachel, Roland Wiesendanger, and Jens Wiebe, "Topological shiba bands in artificial spin chains on superconductors," Nature Physics **17**, 943–948 (2021).

[24] Felix Lüpke, Dacen Waters, Sergio C. de la Barrera, Michael Widom, David G. Mandrus, Jiaqiang Yan, Randall M. Feenstra, and Benjamin M. Hunt, "Proximity-induced superconducting gap in the quantum spin hall edge state of monolayer WTe2," Nature Physics **16**, 526–530 (2020).

[25] Berthold Jäck, Yonglong Xie, Jian Li, Sangjun Jeon, B. Andrei Bernevig, and Ali Yazdani, "Observation of a majorana zero mode in a topologically protected edge channel," Science **364**, 1255–1259 (2019).

[26] Shawulienu Kezilebieke, Md Nurul Huda, Viliam Vaňo, Markus Aapro, Somesh C. Ganguli, Orlando J. Silveira, Szczepan Głodzik, Adam S. Foster, Teemu Ojanen, and Peter Liljeroth, "Topological superconductivity in a van der waals heterostructure," Nature **588**, 424–428 (2020).

[27] Shawulienu Kezilebieke, Orlando J. Silveira, Md N. Huda, Viliam Vaňo, Markus Aapro, Somesh Chandra Ganguli, Jouko Lahtinen, Rhodri Mansell, Sebastiaan Dijken, Adam S. Foster, and Peter Liljeroth, "Electronic and magnetic characterization of epitaxial CrBr 3 monolayers on a superconducting substrate," Advanced Materials **33**, 2006850 (2021).

[28] Shawulienu Kezilebieke, Viliam Vaňo, Md N. Huda, Markus Aapro, Somesh C. Ganguli, Peter Liljeroth, and Jose L. Lado, "Moiré-enabled topological superconductivity," Nano Letters **22**, 328–333 (2022).

[29] A. K. Geim and I. V. Grigorieva, "Van der waals heterostructures," Nature **499**, 419–425 (2013).

[30] Yuan Liu, Nathan O. Weiss, Xidong Duan, Hung-Chieh Cheng, Yu Huang, and Xiangfeng Duan, "Van der waals heterostructures and devices," Nature Reviews Materials **1** (2016), 10.1038/natrevmats.2016.42.

[31] J. M. B. Lopes dos Santos, N. M. R. Peres, and A. H. Castro Neto, "Graphene bilayer with a twist: Electronic structure," Phys. Rev. Lett. **99**, 256802 (2007).

[32] E. Suárez Morell, J. D. Correa, P. Vargas, M. Pacheco, and Z. Barticevic, "Flat bands in slightly twisted bilayer graphene: Tight-binding calculations," Phys. Rev. B **82**, 121407 (2010).

[33] R. Bistritzer and A. H. MacDonald, "Moire bands in twisted double-layer graphene," Proceedings of the National Academy of Sciences **108**, 12233–12237 (2011).

[34] Shiang Fang and Efthimios Kaxiras, "Electronic structure theory of weakly interacting bilayers," Phys. Rev. B **93**, 235153 (2016).

[35] A. O. Sboychakov, A. L. Rakhmanov, A. V. Rozhkov, and Franco Nori, "Electronic spectrum of twisted bilayer graphene," Phys. Rev. B **92**, 075402 (2015).

[36] Tiancheng Song, Qi-Chao Sun, Eric Anderson, Chong Wang, Jimin Qian, Takashi Taniguchi, Kenji Watanabe, Michael A. McGuire, Rainer Stöhr, Di Xiao, Ting Cao, Jörg Wrachtrup, and Xiaodong Xu, "Direct visualization of magnetic domains and moiré magnetism in twisted 2d magnets," Science **374**, 1140–1144 (2021).

[37] Trond I. Andersen, Giovanni Scuri, Andrey Sushko, Kristiaan De Greve, Jiho Sung, You Zhou, Dominik S. Wild, Ryan J. Gelly, Hoseok Heo, Damien Bérubé, Andrew Y. Joe, Luis A. Jauregui, Kenji Watanabe, Takashi Taniguchi, Philip Kim, Hongkun Park, and Mikhail D. Lukin, "Excitons in a reconstructed moiré potential in twisted WSe2/WSe2 homobilayers," Nature Materials **20**, 480–487 (2021).

[38] Eduardo V. Castro, María P. López-Sancho, and María A. H. Vozmediano, "New type of vacancy-induced localized states in multilayer graphene," Phys. Rev. Lett. **104**, 036802 (2010).

[39] M. M. Ugeda, I. Brihuega, F. Guinea, and J. M. Gómez-Rodríguez, "Missing atom as a source of carbon magnetism," Phys. Rev. Lett. **104**, 096804 (2010).

[40] Lan Nguyen, Hannu-Pekka Komsa, Ekaterina Khestanova, Reza J. Kashtiban, Jonathan J. P. Peters, Sean Lawlor, Ana M. Sanchez, Jeremy Sloan, Roman V. Gorbachev, Irina V. Grigorieva, Arkady V. Krasheninnikov, and Sarah J. Haigh, "Atomic defects and doping of monolayer NbSe2," ACS Nano **11**, 2894–2904 (2017).

[41] Shanshan Wang, Alex Robertson, and Jamie H. Warner, "Atomic structure of defects and dopants in 2d layered transition metal dichalcogenides," Chemical Society Reviews **47**, 6764–6794 (2018).

[42] Sara Barja, Sivan Refaely-Abramson, Bruno Schuler, Diana Y. Qiu, Artem Pulkin, Sebastian Wickenburg, Hyejin Ryu, Miguel M. Ugeda, Christoph Kastl, Christopher Chen, Choongyu Hwang, Adam Schwartzberg, Shaul Aloni, Sung-Kwan Mo, D. Frank Ogletree, Michael F. Crommie, Oleg V. Yazyev, Steven G. Louie, Jeffrey B. Neaton, and Alexander Weber-Bargioni, "Identifying substitutional oxygen as a prolific point defect in monolayer transition metal dichalcogenides," Nature Communications **10** (2019), 10.1038/s41467-019-11342-2.

[43] A. V. Balatsky, I. Vekhter, and Jian-Xin Zhu, "Impurity-induced states in conventional and unconventional superconductors," Rev. Mod. Phys. **78**, 373–433 (2006).

[44] A. M. Black-Schaffer, A. V. Balatsky, and J. Fransson, "Filling of magnetic-impurity-induced gap in topological insulators by potential scattering," Phys. Rev. B **91**, 201411 (2015).

[45] I. C. Fulga, B. van Heck, M. Burrello, and T. Hyart, "Effects of disorder on coulomb-assisted braiding of majorana zero modes," Phys. Rev. B **88**, 155435 (2013).

[46] Lukas Kimme and Timo Hyart, "Existence of zero-energy impurity states in different classes of topological insulators and superconductors and their relation to topological phase transitions," Phys. Rev. B **93**, 035134 (2016).

[47] Kim Pöyhönen, Alex Weststrom, and Teemu Ojanen, "Topological superconductivity in ferromagnetic atom chains beyond the deep-impurity regime," Phys. Rev. B **93**, 014517 (2016).

[48] V Kaladzhyan, C Bena, and P Simon, "Asymptotic behavior of impurity-induced bound states in low-dimensional topological superconductors," Journal of Physics: Condensed Matter **28**, 485701 (2016).

[49] Yuan-Yen Tai, Hongchul Choi, Towfiq Ahmed, C. S. Ting, and Jian-Xin Zhu, "Edge states and local electronic structure around an adsorbed impurity in a topological superconductor," Phys. Rev. B **92**, 174514 (2015).

[50] Ivan Brihuega and Felix Yndurain, "Selective hydrogen adsorption in graphene rotated bilayers," The Journal of Physical Chemistry B **122**, 595–600 (2017).

[51] Aline Ramires and Jose L. Lado, "Impurity-induced triple point fermions in twisted bilayer graphene," Phys. Rev. B **99**, 245118 (2019).

[52] Alejandro Lopez-Bezanilla and J. L. Lado, "Electrical band flattening, valley flux, and superconductivity in twisted trilayer graphene," Phys. Rev. Research **2**, 033357 (2020).

[53] Alejandro Lopez-Bezanilla and J. L. Lado, "Defect-induced magnetism and yu-shiba-rusinov states in twisted bilayer graphene," Phys. Rev. Materials **3**, 084003 (2019).

[54] Thomas Naimer, Klaus Zollner, Martin Gmitra, and Jaroslav Fabian, "Twist-angle dependent proximity induced spin-orbit coupling in graphene/transition metal dichalcogenide heterostructures," Phys. Rev. B **104**, 195156 (2021).

[55] Klaus Zollner and Jaroslav Fabian, "Bilayer graphene encapsulated within monolayers of ws_2 or $cr_2ge_2te_6$: Tunable proximity spin-orbit or exchange coupling," Phys. Rev. B **104**, 075126 (2021).

[56] Petra Högl, Tobias Frank, Klaus Zollner, Denis Kochan, Martin Gmitra, and Jaroslav Fabian, "Quantum anomalous hall effects in graphene from proximity-induced uniform and staggered spin-orbit and exchange coupling," Phys. Rev. Lett. **124**, 136403 (2020).

[57] Xiangting Hu, Ning Mao, Hao Wang, Ying Dai, Baibiao Huang, and Chengwang Niu, "Quantum spin hall effect in antiferromagnetic topological heterobilayers," Phys. Rev. B **103**, 085109 (2021).

[58] Bogdan Karpiak, Aron W Cummings, Klaus Zollner, Marc Vila, Dmitrii Khokhriakov, Anamul Md Hoque, André Dankert, Peter Svedlindh, Jaroslav Fabian, Stephan Roche, and Saroj P Dash, "Magnetic proximity in a van der waals heterostructure of magnetic insulator and graphene," 2D Materials **7**, 015026 (2019).

[59] Giovanni Cantele, Dario Alfè, Felice Conte, Vittorio Cataudella, Domenico Ninno, and Procolo Lucignano, "Structural relaxation and low-energy properties of twisted bilayer graphene," Phys. Rev. Research **2**, 043127 (2020).

[60] Long Zhang, Zhe Zhang, Fengcheng Wu, Danqing Wang, Rahul Gogna, Shaocong Hou, Kenji Watanabe, Takashi Taniguchi, Krishnamurthy Kulkarni, Thomas Kuo, Stephen R. Forrest, and Hui Deng, "Twist-angle dependence of moiré excitons in WS2/MoSe2 heterobilayers," Nature Communications **11** (2020), 10.1038/s41467-020-19466-6.

[61] Nicolas Ubrig, Zhe Wang, Jérémie Teyssier, Takashi Taniguchi, Kenji Watanabe, Enrico Giannini, Alberto F Morpurgo, and Marco Gibertini, "Low-temperature monoclinic layer stacking in atomically thin CrI3 crystals," 2D Materials **7**, 015007 (2019).

[62] Daniel J. Trainer, BaoKai Wang, Fabrizio Bobba, Noah Samuelson, Xiaoxing Xi, John Zasadzinski, Jouko Nieminen, Arun Bansil, and Maria Iavarone, "Proximity-induced superconductivity in monolayer MoS2," ACS Nano **14**, 2718–2728 (2020).

[63] M. Kim, P. Kumaravadivel, J. Birkbeck, W. Kuang, S. G. Xu, D. G. Hopkinson, J. Knolle, P. A. McClarty, A. I. Berdyugin, M. Ben Shalom, R. V. Gorbachev, S. J. Haigh, S. Liu, J. H. Edgar, K. S. Novoselov, I. V. Grigorieva, and A. K. Geim, "Micromagnetometry of two-dimensional ferromagnets," Nature Electronics **2**, 457–463 (2019).

[64] Bevin Huang, Genevieve Clark, Efrén Navarro-Moratalla, Dahlia R. Klein, Ran Cheng, Kyle L. Seyler, Ding Zhong, Emma Schmidgall, Michael A. McGuire, David H. Cobden, Wang Yao, Di Xiao, Pablo Jarillo-Herrero, and Xiaodong Xu, "Layer-dependent ferromagnetism in a van der waals crystal down to the monolayer limit," Nature **546**, 270–273 (2017).

[65] Thomas A. Tartaglia, Joseph N. Tang, Jose L. Lado, Faranak Bahrami, Mykola Abramchuk, Gregory T. McCandless, Meaghan C. Doyle, Kenneth S. Burch, Ying Ran, Julia Y. Chan, and Fazel Tafti, "Accessing new magnetic regimes by tuning the ligand spin-orbit coupling in van der waals magnets," Science Advances **6** (2020), 10.1126/sciadv.abb9379.

[66] Miguel M. Ugeda, Aaron J. Bradley, Yi Zhang, Seita Onishi, Yi Chen, Wei Ruan, Claudia Ojeda-Aristizabal, Hyejin Ryu, Mark T. Edmonds, Hsin-Zon Tsai, Alexander Riss, Sung-Kwan Mo, Dunghai Lee, Alex Zettl, Zahid Hussain, Zhi-Xun Shen, and Michael F. Crommie, "Characterization of collective ground states in single-layer NbSe2," Nature Physics **12**, 92–97 (2015).

[67] Rusen Yan, Guru Khalsa, Brian T Schaefer, Alexander Jarjour, Sergei Rouvimov, Katja C Nowack, Huili G Xing, and Debdeep Jena, "Thickness dependence of superconductivity in ultrathin NbS2," Applied Physics Express **12**, 023008 (2019).

[68] Efrén Navarro-Moratalla, Joshua O. Island, Samuel Mañas-Valero, Elena Pinilla-Cienfuegos, Andres Castellanos-Gomez, Jorge Quereda, Gabino Rubio-Bollinger, Luca Chirolli, Jose Angel Silva-Guillén, Nicolás Agraït, Gary A. Steele, Francisco Guinea, Herre S. J. van der Zant, and Eugenio Coronado, "Enhanced superconductivity in atomically thin TaS2," Nature Communications **7** (2016), 10.1038/ncomms11043.

[69] Chao-Sheng Lian, Christoph Heil, Xiaoyu Liu, Chen Si, Feliciano Giustino, and Wenhui Duan, "Coexistence of superconductivity with enhanced charge density wave order in the two-dimensional limit of TaSe2," The Journal of Physical Chemistry Letters **10**, 4076–4081 (2019).

[70] Kun Zhao, Haicheng Lin, Xiao Xiao, Wantong Huang, Wei Yao, Mingzhe Yan, Ying Xing, Qinghua Zhang, Zi-Xiang Li, Shintaro Hoshino, Jian Wang, Shuyun Zhou, Lin Gu, Mohammad Saeed Bahramy, Hong Yao, Naoto Nagaosa, Qi-Kun Xue, Kam Tuen Law, Xi Chen, and Shuai-Hua Ji, "Disorder-induced multifractal superconductivity in monolayer niobium dichalcogenides," Nature Physics **15**, 904–910 (2019).

[71] Maryam Khosravian and J. L. Lado, "Quasiperiodic criticality and spin-triplet superconductivity in superconductor-antiferromagnet moiré patterns," Phys. Rev. Research **3**, 013262 (2021).

[72] D. Soriano, C. Cardoso, and J. Fernández-Rossier, "Interplay between interlayer exchange and stacking in CrI3 bilayers," Solid State Communications **299**, 113662 (2019).

[73] Nikhil Sivadas, Satoshi Okamoto, Xiaodong Xu, Craig. J. Fennie, and Di Xiao, "Stacking-dependent magnetism in bilayer CrI3," Nano Letters **18**, 7658–7664 (2018).

[74] P. G. De Gennes, *Superconductivity of Metals and Alloys* (CRC Press, 2018).

[75] A. I. Buzdin, "Proximity effects in superconductor-ferromagnet heterostructures," Rev. Mod. Phys. **77**, 935–976 (2005).

[76] Y. Noat, J. A. Silva-Guillén, T. Cren, V. Cherkez, C. Brun, S. Pons, F. Debontridder, D. Roditchev, W. Sacks, L. Cario, P. Ordejón, A. García, and E. Canadell, "Quasiparticle spectra of $2h - \mathrm{nbse}_2$: Two-band superconductivity and the role of tunneling selectivity," Phys. Rev. B **92**, 134510 (2015).

[77] Zhong Lin, Bruno R Carvalho, Ethan Kahn, Ruitao Lv, Rahul Rao, Humberto Terrones, Marcos A Pimenta, and Mauricio Terrones, "Defect engineering of two-dimensional transition metal dichalcogenides," 2D Materials **3**, 022002 (2016).

[78] Soumyajyoti Haldar, Hakkim Vovusha, Manoj Kumar Yadav, Olle Eriksson, and Biplab Sanyal, "Systematic study of structural, electronic, and optical properties of atomic-scale defects in the two-dimensional transition metal dichalcogenides mX_2 ($m =$ Mo, w; $x =$ S, se, te)," Phys. Rev. B **92**, 235408 (2015).

[79] Masoud Mahjouri-Samani, Liangbo Liang, Akinola Oyedele, Yong-Sung Kim, Mengkun Tian, Nicholas Cross, Kai Wang, Ming-Wei Lin, Abdelaziz Boulesbaa, Christopher M. Rouleau, Alexander A. Puretzky, Kai Xiao, Mina Yoon, Gyula Eres, Gerd Duscher, Bobby G. Sumpter, and David B. Geohegan, "Tailoring vacancies far beyond intrinsic levels changes the carrier type and optical response in monolayer MoSe2-x crystals," Nano Letters **16**, 5213–5220 (2016).

[80] Mohnish Pandey, Filip A. Rasmussen, Korina Kuhar, Thomas Olsen, Karsten W. Jacobsen, and Kristian S. Thygesen, "Defect-tolerant monolayer transition metal dichalcogenides," Nano Letters **16**, 2234–2239 (2016).

[81] Lijun Li, Xiaoyu Deng, Zhen Wang, Yu Liu, Milinda Abeykoon, Eric Dooryhee, Aleksandra Tomic, Yanan Huang, John B. Warren, Emil S. Bozin, Simon J. L. Billinge, Yuping Sun, Yimei Zhu, Gabriel Kotliar, and Cedomir Petrovic, "Superconducting order from disorder in 2h-TaSe 2- x s x," npj Quantum Materials **2** (2017), 10.1038/s41535-017-0016-9.

[82] P.W. Anderson, "Theory of dirty superconductors," Journal of Physics and Chemistry of Solids **11**, 26–30 (1959).

[83] Aline Ramires and Manfred Sigrist, "Identifying detrimental effects for multiorbital superconductivity: Application to sr$_2$ruo$_4$," Phys. Rev. B **94**, 104501 (2016).

[84] Aline Ramires, Daniel F. Agterberg, and Manfred Sigrist, "Tailoring T_c by symmetry principles: The concept of superconducting fitness," Phys. Rev. B **98**, 024501 (2018).

[85] Aline Ramires, "Nonunitary Superconductivity in Complex Quantum Materials," arXiv e-prints , arXiv:2202.12178 (2022), arXiv:2202.12178 [cond-mat.supr-con].

[86] Niklas M. Gergs, Lars Fritz, and Dirk Schuricht, "Topological order in the kitaev/majorana chain in the presence of disorder and interactions," Phys. Rev. B **93**, 075129 (2016).

[87] Suraj S. Hegde and Smitha Vishveshwara, "Majorana wave-function oscillations, fermion parity switches, and disorder in kitaev chains," Phys. Rev. B **94**, 115166 (2016).

[88] Elsa Prada, Pablo San-Jose, Michiel W. A. de Moor, Attila Geresdi, Eduardo J. H. Lee, Jelena Klinovaja, Daniel Loss, Jesper Nyg**r**ard, Ramón Aguado, and Leo P. Kouwenhoven, "From andreev to majorana bound states in hybrid superconductor–semiconductor nanowires," Nature Reviews Physics **2**, 575–594 (2020).

[89] Lionel Andersen, Aline Ramires, Zhiwei Wang, Thomas Lorenz, and Yoichi Ando, "Generalized anderson's theorem for superconductors derived from topological insulators," Science Advances **6** (2020), 10.1126/sciadv.aay6502.

[90] Bastian Zinkl and Aline Ramires, "Sensitivity of superconducting states to the impurity location in layered materials," arXiv e-prints , arXiv:2201.05045 (2022), arXiv:2201.05045 [cond-mat.supr-con].

[91] J L Lado and J Fernández-Rossier, "Unconventional yu–shiba–rusinov states in hydrogenated graphene," 2D Materials **3**, 025001 (2016).

[92] Guangze Chen and J. L. Lado, "Impurity-induced resonant spinon zero modes in dirac quantum spin liquids," Phys. Rev. Research **2**, 033466 (2020).

[93] Eva Liebhaber, Sergio Acero González, Rojhat Baba, Gaël Reecht, Benjamin W. Heinrich, Sebastian Rohlf, Kai Rossnagel, Felix von Oppen, and Katharina J. Franke, "Yu–shiba–rusinov states in the charge-density modulated superconductor NbSe2," Nano Letters **20**, 339–344 (2019).

[94] M P Lopez Sancho, J M Lopez Sancho, J M L Sancho, and J Rubio, "Highly convergent schemes for the calculation of bulk and surface green functions," Journal of Physics F: Metal Physics **15**, 851–858 (1985).

[95] Cyrus F. Hirjibehedin, Christopher P. Lutz, and Andreas J. Heinrich, "Spin coupling in engineered atomic structures," Science **312**, 1021–1024 (2006).

[96] F. E. Kalff, M. P. Rebergen, E. Fahrenfort, J. Girovsky, R. Toskovic, J. L. Lado, J. Fernández-Rossier, and A. F. Otte, "A kilobyte rewritable atomic memory," Nature Nanotechnology **11**, 926–929 (2016).

[97] Deung-Jang Choi, Nicolas Lorente, Jens Wiebe, Kirsten von Bergmann, Alexander F. Otte, and Andreas J. Heinrich, "Colloquium: Atomic spin chains on surfaces," Rev. Mod. Phys. **91**, 041001 (2019).

[98] Robert Drost, Teemu Ojanen, Ari Harju, and Peter Liljeroth, "Topological states in engineered atomic lattices," Nature Physics **13**, 668–671 (2017).

[99] Marlou R. Slot, Thomas S. Gardenier, Peter H. Jacobse, Guido C. P. van Miert, Sander N. Kempkes, Stephan J. M. Zevenhuizen, Cristiane Morais Smith, Daniel Vanmaekelbergh, and Ingmar Swart, "Experimental realization and characterization of an electronic lieb lattice," Nature Physics **13**, 672–676 (2017).

[100] Kai Yang, Soo-Hyon Phark, Yujeong Bae, Taner Esat, Philip Willke, Arzhang Ardavan, Andreas J. Heinrich, and Christopher P. Lutz, "Probing resonating valence bond states in artificial quantum magnets," Nature Communications **12** (2021), 10.1038/s41467-021-21274-5.

[101] Felix von Oppen and Katharina J. Franke, "Yu-shiba-rusinov states in real metals," Phys. Rev. B **103**, 205424 (2021).

[102] Héctor González-Herrero, José M. Gómez-Rodríguez,

Pierre Mallet, Mohamed Moaied, Juan José Palacios, Carlos Salgado, Miguel M. Ugeda, Jean-Yves Veuillen, Félix Yndurain, and Iván Brihuega, "Atomic-scale control of graphene magnetism by using hydrogen atoms," Science **352**, 437–441 (2016).

[103] Md Nurul Huda, Shawulienu Kezilebieke, and Peter Liljeroth, "Designer flat bands in quasi-one-dimensional atomic lattices," Phys. Rev. Research **2**, 043426 (2020).

[104] Shawulienu Kezilebieke, Marc Dvorak, Teemu Ojanen, and Peter Liljeroth, "Coupled yu–shiba–rusinov states in molecular dimers on NbSe2," Nano Letters **18**, 2311–2315 (2018).

[105] Shawulienu Kezilebieke, Rok Žitko, Marc Dvorak, Teemu Ojanen, and Peter Liljeroth, "Observation of coexistence of yu-shiba-rusinov states and spin-flip excitations," Nano Letters **19**, 4614–4619 (2019).

[106] Doru Sticlet and Cristian Morari, "Topological superconductivity from magnetic impurities on monolayer nbse$_2$," Phys. Rev. B **100**, 075420 (2019).

[107] Mit H. Naik and Manish Jain, "Ultraflatbands and shear solitons in moiré patterns of twisted bilayer transition metal dichalcogenides," Phys. Rev. Lett. **121**, 266401 (2018).